

# Optical-parametric oscillation in photonic-crystal ring resonators

JENNIFER A. BLACK,<sup>1,\*</sup> GRANT BRODNIK,<sup>1,2</sup> HAIXIN LIU,<sup>1,2</sup> SU-PENG YU,<sup>1,2</sup> DAVID R. CARLSON,<sup>1,3</sup> JIZHAO ZANG,<sup>1,2</sup> TRAVIS C. BRILES,<sup>1</sup> AND SCOTT B. PAPP<sup>1,2</sup>

<sup>1</sup>Time and Frequency Division, National Institute of Standards and Technology, Boulder, Colorado 80305, USA

<sup>2</sup>Department of Physics, University of Colorado, Boulder, Colorado 80309, USA

<sup>3</sup>Octave Photonics, Louisville, Colorado 80027, USA

\*Corresponding author: jennifer.black@nist.gov

Received 30 June 2022; revised 22 September 2022; accepted 23 September 2022; published 20 October 2022

By-design access to laser wavelength, especially with integrated photonics, is critical to advance quantum sensors, such as optical clocks and quantum-information systems, and open opportunities in optical communication. Semiconductor-laser gain provides exemplary efficiency and integration but merely in developed wavelength bands. Alternatively, nonlinear optics requires control of phase matching, but the principle of nonlinear conversion of a pump laser to a designed wavelength is extensible. We report on laser-wavelength access by versatile customization of optical-parametric oscillation (OPO) with a photonic-crystal ring resonator (PhCR). Leveraging the exquisite control of laser propagation provided by a photonic crystal in a traveling-wave ring resonator, we enable OPO generation across a wavelength range of 1234–2093 nm with a 1550-nm pump and 1016–1110 nm with a 1064-nm pump. Moreover, our platform offers pump-to-sideband conversion efficiency of >10% and negligible additive optical-frequency noise across the output range. From laser design to simulation of nonlinear dynamics, we use a Lugiato–Lefever framework that predicts the system characteristics, including bidirectional OPO generation in the PhCR and conversion efficiency in agreement with our observations. Our experiments introduce broadband lasers by design with PhCR OPOs, providing critical functionalities in integrated photonics.

<https://doi.org/10.1364/OPTICA.469210>

## 1. INTRODUCTION

Advances in laser applications especially in fluctuating environments and with less developed spectral ranges drives innovation in laser and integrated photonics technologies. For example, quantum-based sensors [1], quantum-information systems [2], atomic and molecular spectroscopy [3], data communication [4], and photonic-signal generation [5] require diverse laser-wavelength access to enhance performance and enable novel application opportunities. Hence, the development of widely deployable laser sources that support wavelength customization would be broadly utilized. Laser technologies based on solid-state materials, doped optical fibers, and semiconductor gain with bulk cavities are commercially mature with well-understood cost and performance trade-offs. Monolithically integrated semiconductor lasers satisfy a substantial range of applications; however, no semiconductor material offers sufficiently low optical loss to support narrow spectral linewidth commensurate with bulk and fiber lasers [6]. Heterogeneously integrated lasers with fabrication on a common substrate have been developed in widely used spectral ranges, and leveraging low loss waveguide materials has enabled narrow linewidth and ultraprecise laser stabilization [7]. However, heterogeneous laser fabrication is exceptionally complex limiting wavelength access. In the context of these developments,

nonlinear wavelength conversion of a pump source by use of integrated photonics is a flexible tool to expand the palette of any laser platform.

Optical-parametric oscillation (OPO) in Kerr ring resonators is ubiquitous, transforming the flat state of a continuous-wave pump laser to the Turing pattern composed of a few wavelengths [8–10]. In this case, phase matching for OPO is intrinsic, owing to the balance between Kerr frequency shifts and anomalous group-velocity dispersion (GVD). Moreover, the Turing pattern is merely one portion of the phase diagram that describes extended patterns and states of the intracavity field that may be leveraged for laser and frequency-comb generation [11–15]. Through GVD engineering via waveguide geometry in advanced integrated nonlinear photonics platforms, it is possible to control the phase matching that determines the output frequency of an OPO laser. This technique in Kerr ring resonator OPOs has been explored with silica [16,17], aluminum nitride [18], and silicon nitride [19,20]. Photonic-crystal (PhC) devices, which enable manipulation of laser propagation in a medium [21], offer a powerful control of phase matching for nonlinear optics. PhC tailoring of the resonator mode structure is enhanced by high finesse. PhCs have been used in several modalities to support OPO, including the case of a resonator with PhC reflectors connected by a nearly arbitrary waveguide [22] and a suspended slab mode resonator defined by

a PhC structure [23]. PhCs can support resonator OPO through both phase matching and resonator finesse control. OPOs with integrated  $\chi^{(2)}$  ring resonators have also been explored through a more challenging phase-matching process of the pump, signal, and idler [24,25].

Here we introduce a laser platform based on degenerate four-wave-mixing OPO in a photonic-crystal ring resonator (PhCR). We exploit a PhC structure to control laser propagation without loss at the pump wavelength of the OPO; whereas, the waveguide ring resonator offers a broadband high finesse mode structure to support the signal and idler modes of the OPO. Our devices are inscribed with an edgeless nanopattern on the inner wall that opens a photonic bandgap (BG) for the single azimuthal mode that we excite with a pump laser. By coupling forward and backward propagations of this one azimuthal mode, we obtain two modes with a frequency shift to higher and lower frequencies compared with the unperturbed mode, respectively. Either the higher or the lower frequency mode directly enables OPO phase matching with respect to a pair of other azimuthal modes to generate signal and idler waves. Hence, the PhCR BG is a single parameter that we use to provide laser-wavelength access across  $>100$  THz from a single-frequency pump laser. Moreover, the forward and backward couplings associated with the PhCR BG creates bidirectional propagation of the OPO laser that we explore with experiment and theory. We report on the properties of this laser platform, including high conversion efficiency of  $>10\%$ , low additive frequency noise in wavelength conversion, and precision output frequency tuning. These properties are comprehensively traced back to PhC control of phase matchings in our PhCRs.

## 2. METHODS

Frequency-matching of resonator modes therefore naturally dictates the OPO output frequencies, and GVD and Kerr frequency shifts are the principal contributions [9]. We quantify OPO frequency matching with the integrated dispersion,

$$D_{\text{int}}(\mu) = \nu_{\mu} - (\nu_0 + \text{FSR} \cdot \mu), \quad (1)$$

where  $\nu_{\mu}$  are the cold-cavity resonator mode frequencies,  $\mu$  is the mode number relative to the pump laser ( $\mu = 0$ ), and FSR is the free-spectral range. We do not account for the Kerr frequency shift, which is twice as large for  $\mu \neq 0$  than the pump mode. The balance of the power-dependent parametric gain and Kerr shift enable OPO in the anomalous GVD regime, which is specialized for OPO frequency matching since  $D_{\text{int}}$  is positive near the pump [10]; whereas, normal GVD does not assist in frequency matching as the directionality of the Kerr shift inhibits phase matching. As we show below, the purpose of our PhCR is to open a BG that uniquely phase matches OPO under a variety of GVDs, providing a mechanism to design lasers for wavelength access. For example, the engineered BG of an otherwise normal GVD PhCR directly phase matches OPO, which is not possible in ordinary ring resonators. We note that PhCRs substantially modify the resonator mode measured by frequency shifts ( $\approx$  GHz) compared to the linewidth (hundreds of megahertz) and the effect on nonlinear optics, although the ring structure primarily guides light in the device.

Degenerate four-wave-mixing based OPO conserves energy and requires phase matching to support appreciable parametric gain. Resonator modes with perfect phase and frequency matching in terms of  $D_{\text{int}}$  satisfy the equation,

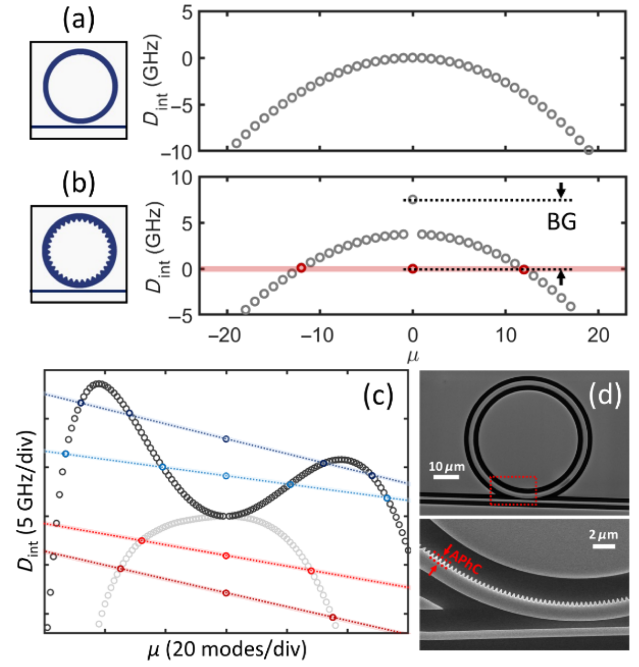


**Fig. 1.** (a) Conventional ring resonator schematic and normal GVD  $D_{\text{int}}$  which does not support OPO phase matching. (b) PhCR schematic and  $D_{\text{int}}$  where a BG is open at the pump, enabling phase matching for OPO on the redshifted PhCR mode. The dotted line highlights the OPO modes satisfying Eq. (2). (c) Two example ring resonator geometries with  $D_{\text{int}}$  including higher-order dispersion terms. Two settings of BG are shown with OPO phase matching (dotted lines) for the blue- and redshifted PhCR modes. (d) Scanning electron microscope image of a full PhCR and zoom in of the PhCR showing the modulation amplitude PhC (APhC).

$$D_{\text{int}}(\mu) = -D_{\text{int}}(-\mu). \quad (2)$$

Practical device design seeks to minimize frequency mismatch of modes symmetric about the pump to less than a ring resonator linewidth ( $\delta$ ),  $D_{\text{int}}(\mu) + D_{\text{int}}(-\mu) < \delta$ . We focus on explaining ring resonator OPO engineering with normal GVD in Fig. 1(a). The quantity  $D_{\text{int}}$  is zero by construction at the pump mode ( $\mu = 0$ ), and we find that  $D_{\text{int}}(\mu \neq 0) < 0$ , which cannot satisfy Eq. (2). However, an analogous PhCR opens a BG on a single ring resonator mode for the pump laser; see Fig. 1(b). Then, by pumping the redshifted (i.e., shifted to lower frequency) PhCR BG-shifted mode ( $\mu = 0$ ), OPO is phase matched at modes  $\mu = \pm 12$  (shaded red box) since the pump mode is frequency shifted in a fashion consistent with an anomalous GVD regime for only the pump mode. Graphically, the modes satisfying Eq. (2) for OPO frequency and phase matching can be represented by a straight line in  $D_{\text{int}}$ , which passes through pump, signal, and idler modes as denoted by the shaded red box in Fig. 1(b). The spacing of the generated OPO frequencies is  $\delta\nu_{\text{OPO}} = \nu_s - \nu_i$ , where  $\nu_s$  and  $\nu_i$  are the generated OPO signal and idler frequencies.

In practice, higher-order dispersion can be a significant consideration, creating the more complex  $D_{\text{int}}$  trends of a realistic PhCR device; see Fig. 1(c). In practice, we tune the GVD using the geometry of the ring resonator. For example, the  $D_{\text{int}}$  in Fig. 1(c) are calculated for experimental ring resonator geometries using tantala ( $\text{Ta}_2\text{O}_5$ ) waveguides with a thickness of 570 nm, top and side air cladding, a  $\text{SiO}_2$  bottom cladding, and a ring radius (RR) of 22.5  $\mu\text{m}$ , which we measure to the center of the ring waveguide. We achieve different GVDs by changing the ring waveguide widths

(RWs), which are 1625 nm and 1710 nm for black and gray  $D_{\text{int}}$  traces in Fig. 1(c), respectively. Here, we present two settings of BG for otherwise anomalous (black) and normal (gray) GVD ring resonators, and we show the OPO-matched modes, using dotted lines which graphically represent solutions to Eq. (2) as described above; red and blue lines signifying OPO on the red- and blueshifted PhCR modes, respectively. The OPO-matched pump, signal, and idler modes satisfy the OPO condition of Eq. (2) [dotted lines in Fig. 1(c)], which is possible despite higher-order dispersion terms as shown in Fig. 1(c). As described above [Fig. 1(b)], we intend to pump the redshifted PhCR mode in an otherwise normal GVD ring resonator, enabling OPO with increasing  $\delta\nu_{\text{OPO}}$  proportional to BG. In an anomalous GVD ring resonators, we intend to pump the blueshifted PhCR mode, providing OPO in two possible branches due to roll over of  $D_{\text{int}}$  at modes further from the pump. To summarize, a BG can be used with arbitrary GVD profiles to enable OPO across a widely tunable spectral range. This contrasts typical GVD constraints for ordinary ring resonator OPO phase matching, which includes the anomalous GVD regime which enables near-pump OPO but results in cascaded four-wave-mixing at higher optical power [16] and the near-zero GVD regime, which enables potentially wide-span OPO but requires careful GVD tuning to access the narrow spectral range near the zero-GVD point [19].

The physical mechanism to open the BG is fabrication of a modulation on the inner wall of the ring resonator. Scanning electron microscope images [Fig. 1(d)] show both the entire PhCR (top) and a zoomed-in image of the PhCR, highlighting the modulation of the inner wall with APHC. The magnitude of the BG depends on APHC, and the optical frequency of the PhC BG depends on the modulation period  $2 \cdot m$ , where  $m$  is the azimuthal mode order of the ring resonator mode where the BG is open.

With the context of PhCR OPOs presented above, we turn our attention to fabrication and experiments that explore formation of lasers and their characteristics. To create PhCRs, we use the  $\text{Ta}_2\text{O}_5$ -integrated nonlinear photonics platform that we have developed [10,26–28].  $\text{Ta}_2\text{O}_5$  offers advantages for PhCR OPOs, including access to high quality factor in the 1064-nm, 1550-nm, and 2000-nm wavelength bands that we explore here and precision control of GVD due to  $<1$  nm film thickness variation across a 75-mm wafer. We use a commercial vendor, FiveNine Optics, to deposit a 570-nm thick  $\text{Ta}_2\text{O}_5$  film on an oxidized silicon wafer by ion-beam sputtering, and our designs are transferred to the  $\text{Ta}_2\text{O}_5$  layer through electron-beam lithography and fluorine inductively coupled plasma-reactive ion etching. Thermal annealing in air for several hours at 500°C reduces oxygen vacancies present in the  $\text{Ta}_2\text{O}_5$  material. Our customized fabrication process yields more than 20 chips with  $\sim 100$  ring resonators per chip in a focused 2-day fabrication period. We use lensed fibers to insert and collect light from the bus waveguides, which use inverse tapers of length 200  $\mu\text{m}$  and width 2.75  $\mu\text{m}$  at the edge of the chips to best mode match to the lensed fibers. We use a straight bus waveguide geometry to couple light to the PhCR, which features a typical intrinsic quality factor of  $2 \times 10^6$ , consistent across the range of BG measured, demonstrating no appreciable loss in the PhCR.

### 3. RESULTS

Figure 2(a) presents our experimental setup for testing lasers created by PhCR OPO, including assessment of bidirectional OPO generation. Our pump laser is an amplified external cavity

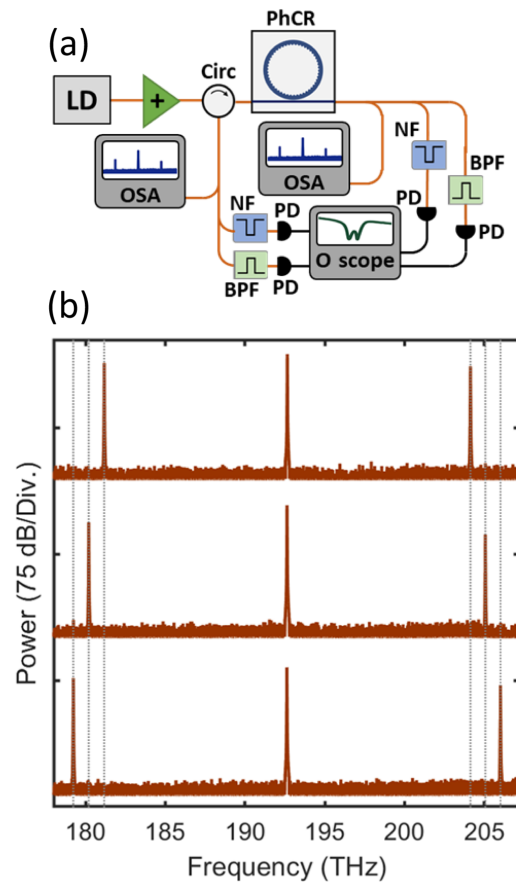


**Fig. 2.** (a) Experimental setup for monitoring bidirectional PhCR OPO. Power from a laser diode (LD) is amplified (+) and passed through a fiber circulator (Circ). Bidirectional OPO generation is monitored on an optical spectrum analyzer (OSA) and filtered (notch- and bandpass-filter: NF, BPF) before monitoring with photodiodes (PDs) and an oscilloscope (O scope). Orange/black paths are optical/electrical. (b) Optical spectra for three settings of BG showing FSR-scale tuning (vertical dashed lines have 1-THz FSR spacing). Top-to-bottom on-chip pump powers are  $29 \pm 2$  mW,  $38 \pm 2$  mW, and  $42 \pm 2$  mW.

diode laser of wavelength in either the 1064-nm or the 1550-nm bands. We monitor the pump power in the forward and backward directions by using a fiber circulator before the PhCR, and optical spectrum analyzers monitor the optical spectra from the PhCR in both directions. We photodetect the pump and OPO power as a function of pump laser detuning in both directions using optical filtering. The principal characteristic of our PhCRs is BG-enabled output laser tuning in which the output is deterministically set in steps of one FSR. Figure 2(b) presents three sample optical spectra demonstrating laser operation where we tune the PhCR OPO output frequencies by tuning BG. The vertical dashed lines are separated by the 1-THz FSR, demonstrating BG-enabled wavelength control.

Figure 3 presents the output frequency from several PhCR OPO devices as a function of BG, emphasizing laser-wavelength access with high conversion efficiency. We find that with nearly the same pump frequency (193 THz), we generate output frequencies (dots) from 143 THz to 243 THz. We also demonstrate PhCR OPO by pumping at 282 THz, accessing frequencies from 278 THz to 286 THz; see the upper broken axis in Fig. 3(a). The solid lines in Fig. 3(a) denote the theoretical phase matching computed with finite element method modeling and Eq. (2) for



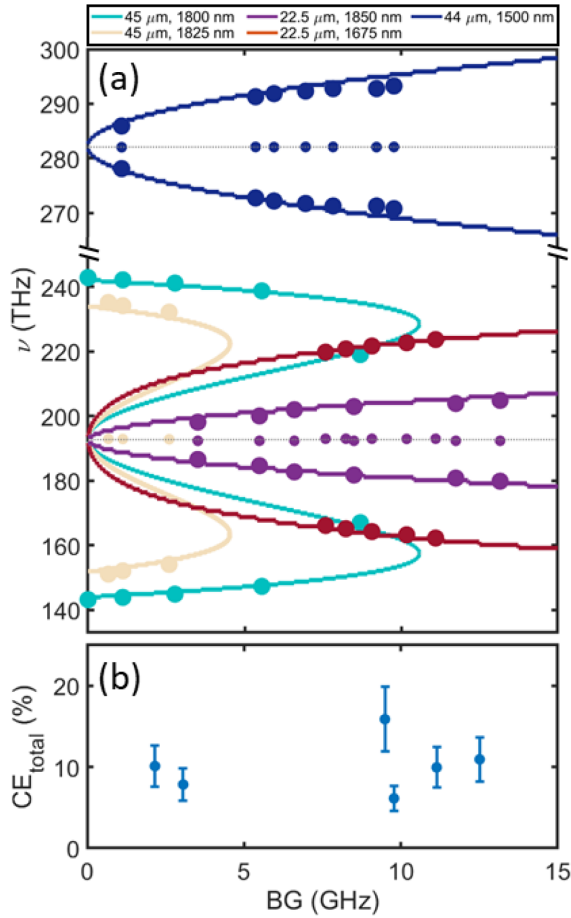


**Fig. 3.** (a) Summary of laser output frequencies versus BG for various ring resonator geometries controlled by RR and RW. The legend presents RR and RW, respectively. Dots (lines) are experimental (theoretical) results. Horizontal dashed lines denote the pump frequency. (b)  $\text{CE}_{\text{total}}$  versus PhCR BG.

a few settings of RR and RW [Fig. 3(a)]. The parabolic trends in Fig. 3(a) (purple, red, and dark blue) denote OPO in otherwise normal GVD ring resonators, which without a PhCR BG would not satisfy Eq. (2) and, therefore, would not generate OPO. The remaining data (turquoise and beige) denote OPO in anomalous GVD ring resonators, demonstrating the two-branch behavior discussed above [see Fig. 1(c)]. Figure 3(a) highlights the versatility of PhCR for OPO generation in vastly different GVD regimes and spectral ranges, controlled by the PhCR BG. Since the PhCR OPO is bidirectional, we observe laser generation in both the forward and the backward directions; hence, we monitor the power propagating in both directions to determine the conversion efficiency from the pump to the OPO output. We calculate the total conversion efficiency ( $\text{CE}_{\text{total}}$ ) as the sum of the optical power generated in the forward and backward directions compared to the input optical power. Note that at higher pump powers, cascaded OPO and other saturation effects that trend toward a frequency comb are possible [29]; therefore, in these measurements, we only consider optical power at our target OPO frequencies. We plot  $\text{CE}_{\text{total}}$  in Fig. 3(b) as a function of BG for ring resonators pumped to  $\sim 1.3$  times the OPO threshold power in ring resonators that are slightly overcoupled with coupling parameter  $K = 3 \pm 1 = (1 + \sqrt{T})/(1 - \sqrt{T})$ , where  $T$  is the transmission on-resonance [30]. The measured threshold powers are between

10- and 70-mW on-chip, and we attribute the range of threshold powers to the unique phase mismatch for a given ring resonator geometry.

We have also explored fine-scale frequency tuning and the frequency linewidth of the PhCR OPO; see Fig. 4. Since our devices require resonant operation, OPO tuning via pump frequency tuning is limited to within a ring resonator linewidth (typically, hundreds of megahertz). For further frequency tuning, we leverage the thermo-optic coefficient of the  $\text{Ta}_2\text{O}_5$  material so that a change in the chip temperature results in approximately  $-1$  GHz/K shift of the PhCR modes [15]. By adjusting the temperature of the chip with a thermoelectric cooler and the frequency of the pump laser, we shift the frequency of the OPO output commensurate with the  $-1$  GHz/K applied shift. Figure 4(a) presents the OPO spectra from two PhCR devices with different BG settings; hence, they produce output at designed wavelengths of 1518 nm, 1595 nm, 1455 nm, and 1672 nm ( $\delta\nu_{\text{OPO}} = 9.53$  THz and 26.74 THz) from a pump at 1555 nm. Specifically with the PhCR device that targets the latter wavelengths, we adjust the temperature in intervals of  $10^\circ\text{C}$  between  $10^\circ\text{C}$  and  $60^\circ\text{C}$  to affect output frequencies tuning with  $dn/dT \approx -(n/\nu) \cdot (d\nu/dT) = 8.8 \times 10^{-6} \text{ K}^{-1}$ , consistent with previous results [27].

We characterize the linewidth of the PhCR OPO lasers, especially additive frequency noise that results from the nonlinear laser generation process itself. We perform the measurements with an unbalanced optical frequency discriminator Mach-Zehnder interferometer (MZI) setup of FSR  $12.8 \pm 0.3$  MHz. In particular, we derive the integrated linewidth after measuring frequency noise using the  $1/\pi$  phase and  $\beta$ -separation techniques [4,31,32], which capture information about high- and low-frequency noises, respectively. Following OPO laser generation, we optically filter the pump, OPO signal, idler, and photodetect the individual wavelengths after propagating through the MZI, and the output voltage from the photodetector is converted to frequency noise; see Fig. 4(c). The pump laser has a  $1/\pi$ -integral linewidth of  $13.7 \pm 0.2$  kHz [Fig. 4(b)] and a  $\beta$ -separation linewidth of  $693 \pm 28$  kHz, quantifying the low-frequency drift present in the pump laser. The OPO signal and idler frequencies have a maximum  $1/\pi$ -integral linewidth of  $34 \pm 1$  kHz and a  $\beta$ -separation linewidth of  $958 \pm 41$  kHz; see Fig. 4(b). We attribute the increase in OPO linewidth to thermorefractive noise (TRN) in the PhCR [33]. TRN jitter of the PhCR mode naturally induces pump detuning noise, which influences the OPO output frequency. Still, TRN couples to nonlinear processes in a relatively complex manner, especially for microcombs with large laser detuning in which the effect has been studied in detail [33]. Our present frequency noise measurements are in order of magnitude agreement with TRN models, accounting for the  $\sim 10$  dB lower TRN due to the smaller thermo-optic coefficient of  $\text{Ta}_2\text{O}_5$ . In future experiments, we would explore the detuning dependence of TRN in PhCR OPOs especially to understand the nonlinear coupling contribution [34,35].

We envision a range of potential applications for our OPO tunable-laser platform especially in addressing requirements for wide laser-wavelength access. To understand both the operational system dynamics and the CE of the pump laser power to OPO output power, we present analysis of output power as a function of the system parameters; see Fig. 5. Importantly, PhCR OPO operates bidirectionally, sending power in both the forward and the backward directions with respect to the pump laser input.

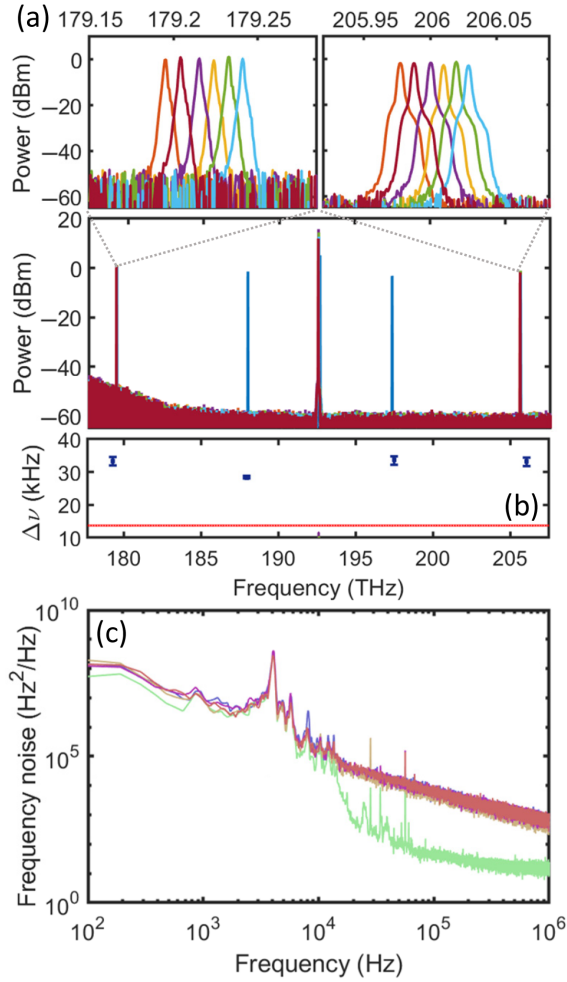


**Fig. 4.** (a) Optical spectra for two different BGs with  $\delta\nu_{\text{OPO}} = 9.53, 26.74$  THz, which are pumped with  $29 \pm 2$  mW and  $56 \pm 3$  mW of on-chip pump power. Top left and right panels demonstrate thermo-optic tuning of OPO output when heated in  $10^\circ\text{C}$  intervals from  $10^\circ\text{C}$  to  $60^\circ\text{C}$ , while the pump laser is on-resonance. (b) Measured OPO  $1/\pi$ -integrated linewidth  $\Delta\nu$  for idler and signal frequencies corresponding to (a) in blue dots. The measured pump laser  $1/\pi$ -integrated linewidth is denoted with red lines. (c) Frequency noise measurements of OPO in (a) and (b). Green is the pump laser (193 THz), purple, gold, mauve, and light red are OPO frequencies 198 THz, 188 THz, 206 THz, and 179 THz, respectively.

Experimentally, we detect OPO power bidirectionally by filtering the pump light as outlined in Fig. 2(a). Figure 5(a) shows experimental OPO power in the forward and the backward directions as a function of detuning relative to the OPO threshold, normalized to the OPO power in the forward direction. We find that, although the relative OPO powers are nearly equal in the forward (red) and backward (blue) directions at certain detuning settings, OPO power can propagate more predominantly in the forward or backward directions. Furthermore, while analyzing these data, we observed that facet reflections play an important role in the forward and backward power balances. In these experiments, we constrain the pump power below that is required for secondary and higher OPO processes and discrete states, such as solitons, which have been explored in detail [10,29]. Indeed, in both experiment and modeling, it is straightforward to maintain a suitable pump power for single signal and idler generations, yielding OPO lasers with low noise and high suppression of side-mode effects; see Fig. 4.

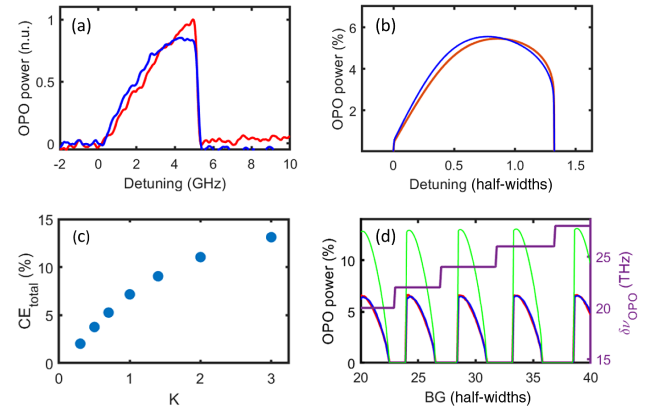


**Fig. 5.** (a) Experimental normalized OPO power in the forward and backward directions (red and blue) for pump power  $\sim 1.3 \times$  OPO threshold as a function of laser detuning (relative to OPO threshold). (b) Theoretical relative OPO power for  $F = 2.28$  in the forward and backward (red and blue) directions as a function of detuning. (c) Theoretical  $\text{CE}_{\text{total}}$  as a function of coupling parameter  $K$  for  $F = 2.28$ . (d) OPO power dependence (left axis red, blue, and green OPO power in forward, backward, and total) and  $\delta\nu_{\text{OPO}}$  (right, purple) as a function of BG.

Studying the distinct transition between the OPO regime and, for example, the dark-to-bright soliton continuum may be of theoretical interest in the future; however, the complex nonlinear dynamics of that transition most likely stand in the way of practical laser and frequency-comb applications.

To better understand the physics of PhCR OPO, we model the system with a pair of Lugiato–Lefever equations (LLE)  $\partial_t \psi = -(1 + i\alpha)\psi - \frac{1}{2}\beta\partial_\theta^2 \psi + i|\psi|^2 \psi + F$ , which describe the forward and backward intracavity fields  $\psi(\theta, t)$ , where  $t$  is time, and  $\theta$  is the angular coordinate along the ring resonator [36]. The parameters  $\alpha$  and  $\beta$  are the laser detuning and dispersion parameters, which are normalized to the PhCR mode linewidth, and  $F$  is the pump field. Parameter  $\beta$  includes the BG, and we incorporate fields propagating in both the forward and backward directions [37]. Our modeling also includes 6.8% reflection of optical power in either direction to reflect realistic experimental parameters, namely, reflections from the chip facets. We model second-order dispersion of  $-0.094$  half-widths/mode and  $F = 2.28$ , which is distributed into both the forward and backward directions. In our model, the theoretical OPO threshold is near  $F = 2$  in which the field splits between forward and backward directions, and the overall dispersion nearly satisfies Eq. (2). However, the OPO threshold depends on the overall pump frequency, dispersion, BG setting ( $\beta$ ), and the amount of field that is reflected towards the PhCR. Figure 5(b) presents theoretical OPO power predictions in the forward and backward directions as a function of laser detuning relative to the onset of OPO ( $F = 2.28$ ) and are in good qualitative agreement with experimental OPO power found in Fig. 5(a). Note that the thermal bistability evident in Fig. 5(a) is not reflected in the theoretical model [Fig. 5(b)] [38]. Figure 5(b) predicts theoretical OPO power conversion  $\sim 5.5\%$  into the forward and backward directions ( $\text{CE}_{\text{total}} \sim 11\%$ ) when  $K = 3$  (overcoupled), which agrees with the experimental results in Fig. 3(b). The full solution of the forward and backward LLE fields, shown in Fig. 5(b), incorporates the BG-induced scattering rate in the PhCR [39] and nonlinear couplings that have been explored recently in the context of injection-locked microcombs [40].

We also theoretically investigate the OPO conversion efficiency as a function of coupling parameter,  $K$ , and BG. We find that at BG settings with small phase mismatch,  $CE_{\text{total}}$  increases with  $K$  as seen in Fig. 5(c) where we use a fixed field  $F = 2.28$  to reflect experimental parameters  $[(2.28/2)^2 = 1.3]$ . Note that, although increasing  $K$  results in higher  $CE_{\text{total}}$ , this also increases the OPO threshold power [41]. Figure 5(d) presents PhCR OPO dynamics as a function of BG with fixed  $F = 2.28$  and  $K = 3$ . The left axis shows the forward (red), backward (blue), and total (green) OPO conversion efficiency. At certain BG [e.g., 20 half-widths in Fig. 5(d)],  $CE_{\text{total}}$  peaks at 13% when the BG setting satisfies Eq. (2). Other values of BG [e.g., 37 half-widths in Fig. 5(d)] provide poor phase matching such that at  $F = 2.28$ , no OPO is possible due to lack of sufficient parametric gain. The right axis in Fig. 5(d) shows  $\delta\nu_{\text{OPO}}$  (purple), demonstrating BG-dependent stepwise tuning of the laser output.

## 4. CONCLUSION

In conclusion, we have presented a platform for laser-wavelength access by use of PhCR OPO. We use a  $\text{Ta}_2\text{O}_5$ -integrated photonic platform to achieve by-design laser access  $>100$  THz of the optical bandwidth with a narrow output linewidth. Our results demonstrate controllable laser wavelength generation with total pump-to-sideband conversion efficiencies  $>10\%$ , which is predicted by bidirectional LLE modeling.

**Funding.** National Science Foundation (OMA-2016244); Air Force Office of Scientific Research (FA9550-20-1-0004); Defense Advanced Research Projects Agency; National Institute of Standards and Technology.

**Acknowledgment.** This work is a contribution of the U.S. Government and is not subject to copyright. Mention of specific companies or trade names is for scientific communication only and does not constitute a specific endorsement by the National Institute of Standards and Technology.

**Disclosures.** David Carlson is a cofounder of Octave Photonics. The remaining authors do not currently have a financial interest in  $\text{Ta}_2\text{O}_5$ -integrated photonics.

**Data availability.** Data underlying the results presented in this paper are not publicly available at this time but may be obtained from the authors upon reasonable request.

## REFERENCES

1. T. Bothwell, C. J. Kennedy, A. Aeppli, D. Kedar, J. M. Robinson, E. Oelker, A. Staron, and J. Ye, "Resolving the gravitational redshift across a millimetre-scale atomic sample," *Nature* **602**, 420–424 (2022).
2. J. M. Pino, J. M. Dreiling, C. Figgatt, J. P. Gaebler, S. A. Moses, M. S. Allman, C. H. Baldwin, M. Foss-Feig, D. Hayes, K. Mayer, C. Ryan-Anderson, and B. Neyenhuis, "Demonstration of the trapped-ion quantum CCD computer architecture," *Nature* **592**, 209–213 (2021).
3. Y. Liu, H. Lin, B. A. Z. Montano, W. Zhu, Y. Zhong, R. Kan, B. Yuan, J. Yu, M. Shao, and H. Zheng, "Integrated near-infrared QEPAS sensor based on a 28 kHz quartz tuning fork for online monitoring of  $\text{CO}_2$  in the greenhouse," *Photoacoustics* **25**, 100332 (2022).
4. G. M. Brodnik, M. W. Harrington, J. H. Dallyn, D. Bose, W. Zhang, L. Stern, P. A. Morton, R. O. Behunin, S. B. Papp, and D. J. Blumenthal, "Optically synchronized fibre links using spectrally pure chip-scale lasers," *Nat. Photonics* **15**, 588–593 (2021).
5. J. Capmany and D. Novak, "Microwave photonics combines two worlds," *Nat. Photonics* **1**, 319–330 (2007).
6. D. Liang and J. E. Bowers, "Recent progress in lasers on silicon," *Nat. Photonics* **4**, 511–517 (2010).
7. L. Stern, W. Zhang, L. Chang, J. Guo, C. Xiang, M. A. Tran, D. Huang, J. D. Peters, D. Kinghorn, J. E. Bowers, and S. B. Papp, "Ultra-precise optical-frequency stabilization with heterogeneous III–V/Si lasers," *Opt. Lett.* **45**, 5275–5278 (2020).
8. X. Lu, S. Rogers, W. C. Jiang, and Q. Lin, "Selective engineering of cavity resonance for frequency matching in optical parametric processes," *Appl. Phys. Lett.* **105**, 151104 (2014).
9. X. Lu, G. Moille, A. Singh, Q. Li, D. A. Westly, A. Rao, S.-P. Yu, T. C. Briles, S. B. Papp, and K. Srinivasan, "Milliwatt-threshold visible-telecom optical parametric oscillation using silicon nanophotonics," *Optica* **6**, 1535–1541 (2019).
10. S.-P. Yu, D. C. Cole, H. Jung, G. T. Moille, K. Srinivasan, and S. B. Papp, "Spontaneous pulse formation in edgeless photonic crystal resonators," *Nat. Photonics* **15**, 461–467 (2021).
11. A. Coillet, I. Balakireva, R. Henriet, K. Saleh, L. Larger, J. M. Dudley, C. R. Menyuk, and Y. K. Chembo, "Azimuthal Turing patterns, bright and dark cavity solitons in Kerr combs generated with whispering-gallery-mode resonators," *IEEE Photon. J.* **5**, 6100409 (2013).
12. A. Pasquazi, M. Peccianti, L. Razzari, D. J. Moss, S. Coen, M. Erkintalo, Y. K. Chembo, T. Hansson, S. Wabnitz, P. Del'Haye, X. Xue, A. M. Weiner, and R. Morandotti, "Micro-combs: a novel generation of optical sources," *Phys. Rep.* **729**, 1–81 (2018).
13. T. J. Kippenberg, A. L. Gaeta, M. Lipson, and M. L. Gorodetsky, "Dissipative Kerr solitons in optical microresonators," *Science* **361**, eaan8083 (2018).
14. D. V. Skryabin, Z. Fan, A. Villois, and D. N. Puzryev, "Threshold of complexity and Arnold tongues in Kerr-ring microresonators," *Phys. Rev. A* **103**, L011502 (2021).
15. D. N. Puzryev and D. V. Skryabin, "Finesse and four-wave mixing in microresonators," *Phys. Rev. A* **103**, 013508 (2021).
16. T. J. Kippenberg, S. M. Spillane, and K. J. Vahala, "Kerr-nonlinearity optical parametric oscillation in an ultrahigh-Q toroid microcavity," *Phys. Rev. Lett.* **93**, 083904 (2004).
17. N. L. B. Sayson, K. E. Webb, S. Coen, M. Erkintalo, and S. G. Murdoch, "Widely tunable optical parametric oscillation in a Kerr microresonator," *Opt. Lett.* **42**, 5190–5193 (2017).
18. Y. Tang, Z. Gong, X. Liu, and H. X. Tang, "Widely separated optical Kerr parametric oscillation in AlN microrings," *Opt. Lett.* **45**, 1124–1127 (2020).
19. X. Lu, G. Moille, A. Rao, D. A. Westly, and K. Srinivasan, "On-chip optical parametric oscillation into the visible: generating red, orange, yellow, and green from a near-infrared pump," *Optica* **7**, 1417–1425 (2020).
20. R. R. Domenegueti, Y. Zhao, X. Ji, M. Martinelli, M. Lipson, A. L. Gaeta, and P. Nussenzveig, "Parametric sideband generation in CMOS-compatible oscillators from visible to telecom wavelengths," *Optica* **8**, 316–322 (2021).
21. D. Lindley, "Landmarks—the birth of photonic crystals," *Physics* **6**, 94 (2013).
22. S.-P. Yu, H. Jung, T. C. Briles, K. Srinivasan, and S. B. Papp, "Photonic-crystal-reflector nanoresonators for Kerr-frequency combs," *ACS Photon.* **6**, 2083–2089 (2019).
23. G. Marty, S. Combrié, F. Raineri, and A. De Rossi, "Photonic crystal optical parametric oscillator," *Nat. Photonics* **15**, 53–58 (2021).
24. J. Lu, A. A. Sayem, Z. Gong, J. B. Surya, C.-L. Zou, and H. X. Tang, "Ultralow-threshold thin-film lithium niobate optical parametric oscillator," *Optica* **8**, 539–544 (2021).
25. N. Amiune, D. N. Puzryev, V. V. Pankratov, D. V. Skryabin, K. Buse, and I. Breunig, "Optical-parametric-oscillation-based  $\chi^{(2)}$  frequency comb in a lithium niobate microresonator," *Opt. Express* **29**, 41378–41387 (2021).
26. K. F. Lamee, D. R. Carlson, Z. L. Newman, S.-P. Yu, and S. B. Papp, "Nanophotonic tantalum waveguides for supercontinuum generation pumped at 1560 nm," *Opt. Lett.* **45**, 4192–4195 (2020).
27. H. Jung, S.-P. Yu, D. R. Carlson, T. E. Drake, T. C. Briles, and S. B. Papp, "Tantalum Kerr nonlinear integrated photonics," *Optica* **8**, 811–817 (2021).
28. J. A. Black, R. Streater, K. F. Lamee, D. R. Carlson, S.-P. Yu, and S. B. Papp, "Group-velocity-dispersion engineering of tantalum integrated photonics," *Opt. Lett.* **46**, 817–820 (2021).
29. S.-P. Yu, E. Lucas, J. Zang, and S. B. Papp, "A continuum of bright and dark-pulse states in a photonic-crystal resonator," *Nat. Commun.* **13**, 3134 (2022).
30. S. M. Spillane, T. J. Kippenberg, O. J. Painter, and K. J. Vahala, "Ideality in a fiber-taper-coupled microresonator system for application to cavity quantum electrodynamics," *Phys. Rev. Lett.* **91**, 43902 (2003).
31. G. Di Domenico, S. Schilt, and P. Thomann, "Simple approach to the relation between laser frequency noise and laser line shape," *Appl. Opt.* **49**, 4801–4807 (2010).

32. W. Liang, V. S. Ilchenko, D. Eliyahu, A. A. Savchenkov, A. B. Matsko, D. Seidel, and L. Maleki, "Ultralow noise miniature external cavity semiconductor laser," *Nat. Commun.* **6**, 7371 (2015).
33. T. E. Drake, J. R. Stone, T. C. Briles, and S. B. Papp, "Thermal decoherence and laser cooling of Kerr microresonator solitons," *Nat. Photonics* **14**, 480–485 (2020).
34. J. R. Stone, T. C. Briles, T. E. Drake, D. T. Spencer, D. R. Carlson, S. A. Diddams, and S. B. Papp, "Thermal and nonlinear dissipative-soliton dynamics in Kerr-microresonator frequency combs," *Phys. Rev. Lett.* **121**, 063902 (2018).
35. J. R. Stone and S. B. Papp, "Harnessing dispersion in soliton microcombs to mitigate thermal noise," *Phys. Rev. Lett.* **125**, 153901 (2020).
36. C. Godey, I. V. Balakireva, A. Coillet, and Y. K. Chembo, "Stability analysis of the spatiotemporal Lugiato-Lefever model for Kerr optical frequency combs in the anomalous and normal dispersion regimes," *Phys. Rev. A* **89**, 063814 (2014).
37. D. V. Skryabin, "Hierarchy of coupled mode and envelope models for bi-directional microresonators with Kerr nonlinearity," *OSA Continuum* **3**, 1364–1375 (2020).
38. T. Carmon, L. Yang, and K. Vahala, "Dynamical thermal behavior and thermal self-stability of microcavities," *Opt. Express* **12**, 4742–4750 (2004).
39. T. J. Kippenberg, S. M. Spillane, and K. J. Vahala, "Modal coupling in traveling-wave resonators," *Opt. Lett.* **27**, 1669–1671 (2002).
40. T. C. Briles, S.-P. Yu, L. Chang, C. Xiang, J. Guo, D. Kinghorn, G. Moille, K. Srinivasan, J. E. Bowers, and S. B. Papp, "Hybrid InP and SiN integration of an octave-spanning frequency comb," *APL Photon.* **6**, 026102 (2021).
41. J. R. Stone, G. Moille, X. Lu, and K. Srinivasan, "Conversion efficiency in Kerr-microresonator optical parametric oscillators: from three modes to many modes," *Phys. Rev. Appl.* **17**, 024038 (2022).